AIP Journal of Applied Physics

Inductively coupled Ar/CH 4 / H 2 plasmas for low-temperature deposition of ordered carbon nanostructures

I. B. Denysenko, S. Xu, J. D. Long, P. P. Rutkevych, N. A. Azarenkov, and K. Ostrikov

Citation: Journal of Applied Physics **95**, 2713 (2004); doi: 10.1063/1.1642762
View online: http://dx.doi.org/10.1063/1.1642762
View Table of Contents: http://scitation.aip.org/content/aip/journal/jap/95/5?ver=pdfcov
Published by the AIP Publishing

Articles you may be interested in

Optical and electrical characterization of an atmospheric pressure microplasma jet for Ar C H 4 and Ar C 2 H 2 mixtures
J. Appl. Phys. **101**, 103307 (2007); 10.1063/1.2714646

Diagnostic and analytical study on a low-pressure limit of diamond chemical vapor deposition in inductively coupled CO–CH 4 – H 2 plasmas
J. Appl. Phys. **95**, 4463 (2004); 10.1063/1.1686900

Plasma diagnostic study of silicon nitride film growth in a remote Ar–H 2 – N 2 – SiH 4 plasma: Role of N and SiH n radicals
J. Vac. Sci. Technol. A **22**, 96 (2004); 10.1116/1.1631294

Pressure and input power dependence of Ar/N 2 H 2 inductively coupled plasma systems
J. Vac. Sci. Technol. A **19**, 2335 (2001); 10.1116/1.1385904

Mass spectrometric studies of a CH 4 /H 2 microwave plasma under diamond deposition conditions
J. Appl. Phys. **89**, 2543 (2001); 10.1063/1.1346655

AIP Journal of Applied Physics

Journal of Applied Physics is pleased to announce André Anders as its new Editor-in-Chief

[This article is copyrighted as indicated in the article. Reuse of AIP content is subject to the terms at: http://scitation.aip.org/termsconditions. Downloaded to] IP: 131.181.251.131 On: Mon, 14 Jul 2014 22:52:45

HTML ABSTRACT + LINKS

JOURNAL OF APPLIED PHYSICS VOLUME 95, NUMBER 5 1 MARCH 2004

Inductively coupled $Ar/CH_4/H_2$ plasmas for low-temperature deposition of ordered carbon nanostructures

I. B. Denysenko
Plasma Sources and Applications Center, NIE, Nanyang Technological University, 1 Nanyang Walk, 637616 Singapore and School of Physics and Technology, Kharkiv National University, 4 Svobody sq., 61077 Kharkiv, Ukraine

S. Xu,[a] J. D. Long, and P. P. Rutkevych
Plasma Sources and Applications Center, NIE, Nanyang Technological University, 1 Nanyang Walk, 637616 Singapore

N. A. Azarenkov
School of Physics and Technology, Kharkiv National University, 4 Svobody sq., 61077 Kharkiv, Ukraine

K. Ostrikov
Plasma Sources and Applications Center, NIE, Nanyang Technological University, 1 Nanyang Walk, 637616 Singapore and School of Physics, The University of Sydney, Sydney, NSW 2006, Australia

(Received 21 August 2003; accepted 26 November 2003)

The results of numerical simulations, optical emission spectroscopy (OES), and quadrupole mass spectrometry (QMS) of inductively coupled $Ar/CH_4/H_2$ plasmas in the plasma enhanced chemical vapor deposition (PECVD) of self-assembled vertically aligned carbon nanostructures (CNs) are presented. A spatially averaged (global) discharge model is developed to study the densities and fluxes of the radical neutrals and charged species, the effective electron temperature, methane conversion factor under various growth conditions. The numerical results show a remarkable agreement with the OES and QMS data. It is found that the deposited cation fluxes in the PECVD of CNs generally exceed those of the radical neutrals. © *2004 American Institute of Physics.*
[DOI: 10.1063/1.1642762]

I. INTRODUCTION

Carbon nanostructures (CNs) have recently been widely explored for the fabrication of various nano-electronic devices such as electron field emitters,[1] ultrafast transistors,[2] and microelectrochemical systems.[3] Excellent electron field enhancing properties of the CNs are attributed to their unique structural and size-dependent electronic properties.[4] Vertically aligned CNs are also mechanically and chemically robust and are able to emit large currents at low electric fields.[5] The fabrication of large-area ordered carbon nanostructures on conducting substrates is thus essential to achieve a high uniformity of the electron field emission required for the development of vacuum microelectronic devices.

Chemical vapor deposition (CVD) and plasma-enhanced chemical vapor deposition (PECVD) have recently become common carbon nanostructure growth techniques.[6–11] The low-temperature PECVD offers a great deal of vertical alignment and ordering of the CNs due to dc electric fields normal to the growth surface,[12] which favorably differs it from many conventional CVD techniques.

The essential parameters of the PECVD growth of the ordered carbon nanostructures are the feed gases, input power, the nature of catalyst, the substrate temperature T_s, and dc bias V_s.[8,10] To date, many experiments have been focused on the minimization of the growth temperature.[13–16] Recently, capacitively coupled,[17] microwave[14] and inductively coupled plasmas (ICPs)[9,10] of various hydrocarbon-based gas mixtures have successfully been applied for the low-temperature CN growth ($\sim 300–500\,^{\circ}C$). However, capacitively coupled plasmas have not been widely used for this purpose due to strong fluctuating self-bias potentials that somewhat compromise the ability to control the substrate potential. On the other hand, microwave and IC plasmas have recently been considered more attractive in this regard, in particular because of the low-pressure (1–100 mTorr) operation, high electron and ion densities ($10^{11}–10^{12}\ cm^{-3}$), and controllable ion fluxes onto the growth surfaces. Remarkably, the ion bombardment contributes to the fragmetation of catalyst layers and thus plays a key role in the PECVD growth of carbon nanostructures at lower substrate temparatures.[9,16] Our previous studies revealed that numerous vertically aligned carbon nanostructures with high aspect ratios can be grown on large-area (up to 300 cm^2) Ni/Fe/Mn catalyzed silicon substrates in this temperature range using low-frequency inductively coupled $Ar/CH_4/H_2$ plasmas.[10,15]

In order to control the deposition process and improve the emission and other properties of CNs as well as to explore the possibilities for the up scaling to larger growth areas, an insight into the gas-phase plasma processes is crucial. Numerical modeling of the plasma discharges can unambiguously reveal the underlying physics of the deposition process and contribute to the development of the future industrial process specifications.

[a]Author to whom correspondence should be addressed; electronic mail: syxu@nie.edu.sg

 © 2004 American Institute of Physics

[This article is copyrighted as indicated in the article. Reuse of AIP content is subject to the terms at: http://scitation.aip.org/termsconditions. Downloaded to] IP: 131.181.251.131 On: Mon, 14 Jul 2014 22:52:45

Despite the extensive theoretical studies of the plasmas in various hydrocarbon-based feedstock used for the PECVD of diamond-like, graphite-like and amorphous carbon films in the last few decades[18–22] and wide application of the PECVD methods for the CN growth,[7,11,12] the modeling of the low-temparature plasmas in the carbon nanostructure growth only recently attaracted the attention it merits.[8,23,24] However, the existing modeling work[8,23,24] is limited to high-pressure ($\geqslant 3$ Torr) CN growth regimes in methane/acetylene carbon-bearing gases diluted with NH_3/H_2. Hence, the properties of low-pressure (<100 mTorr) plasmas in the PECVD of the ordered carbon nanostructures warrant immediate attention.

This article reports the results of the diagnostics and numerical modeling of the low-frequency ICPs of $Ar/CH_4/H_2$ gas mixture previously used in the PECVD of self-assembled ordered carbon nanotip structures.[10,15] The effects of variation of the discharge control parameters on the methane conversion factor, electron energy, densities of the neutral and charged species, and their fluxes onto a nanostructured surface are studied using a spatially averaged (global) discharge model and are found in a remarkable agreement with the results of the optical emission spectroscopy (OES) and quadrupole mass spectrometry (QMS) measurements.

II. EXPERIMENTAL DETAILS

A low-frequency (~ 0.46 MHz) ICP source has previously been used in the PECVD of CNs.[10,15] In this work, the same conditions are used for the discharge diagnostics and modeling. Below we give the most essential description of the setup. Other experimental details can be found elsewhere.[25–27] A cylindrical stainless steel reactor chamber of the plasma source has the inner diameter $2R=32$ cm and length 23 cm. The chamber is cooled by a continuous water flowing between the inner and outer walls of the chamber. The top plate of the chamber is a fused silica disk, 35 cm in diameter and 1.2 cm thick. A top surface of the stainless steel substrate holder of 17.5 cm diameter is located 11 cm below the bottom surface of the quartz window. A dc voltage in the range of 0–300 V has been applied to the substrate holder to reproduce the CN growth conditions.[10,15] A 450 l/s turbomolecular pump backed by a two-stage rotary pump is used to evacuate the plasma chamber. The inflow rates of the working gases (Ar, H_2 and CH_4) are regulated by MKS mass-flow controllers. The inflow rates of Ar and CH_4 have been varied from 10 to 50 sccm and 3 to 7.5 sccm, respectively. In this work, the hydrogen flow rate was fixed at 12.4 sccm. The total gas pressure in the discharge chamber measured by a MKS Baratron capacitance manometer is in the range of 20–70 mTorr. The rf input power was varied from 1.8 to 3.0 kW. A typical scanning electron micrograph of the PECVD-grown ordered vertically aligned carbon nanotip structure is shown in Fig. 1.

In the previous experiments of our group,[10,15] the argon was used as a multi-purpose dilution gas. First, the bias-controlled argon ion bombardment was enforced at the initial Ni-based catalyst pretreatment stage. Second, the dilution of the working gases with argon facilitates the discharge maintenance and operation due to the outstanding ionization/dissociation capacity of Ar in $CH_4/H_2/Ar$ gas mixtures.[28,29] Meanwhile, the inductive coupling efficiency can be improved as compared with undiluted hydrocarbon/hydrogen mixtures. To this end, the rf coupling in C_xH_y/H_2 discharges features a very strong capacitive component.[9] The use of the pure hydrocarbon feedstock has previously been disfavored due to the enhanced deposition of amorphous carbon. Thus, the role of the H_2/HN_3 diluent is in the predominant removal of the amorphous phase from nanostructured carbon-based films. We note that other inert and hydrogen-bearing gases can be used to dilute the C_xH_y reactive feedstock. However, He is more common in the CNs growth in dielectric barrier discharges at atmospheric pressures.[30]

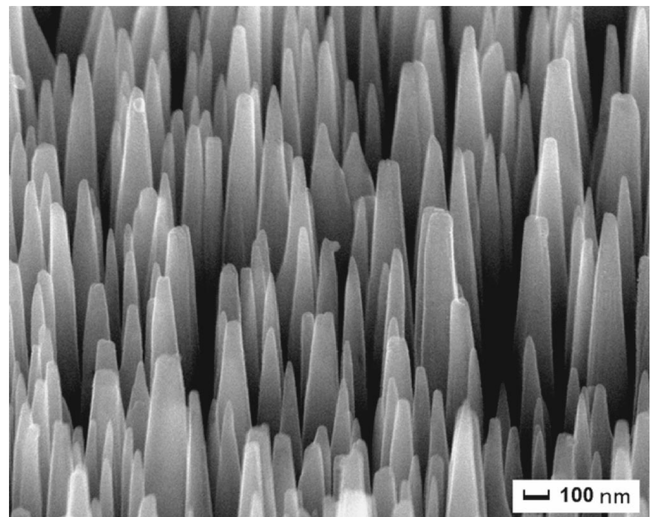

FIG. 1. High-resolution scanning electron micrograph of carbon nanotip array deposited in the IC plasma of $Ar/CH_4/H_2$ mixture at $P_{in}=2$ kW, $J_{Ar}=35$ sccm, $J_{H_2}=12.4$ sccm, $J_{CH_4}=7.5$ sccm, $V_s=-300$ V, and $T_s=300\,°C$.

Variations of neutral densities with the input parameters are measured by a Microvision Plus LP101009 quadrupole mass spectrometer equipped with a Faraday cup detector. A typical distribution of the radical and nonradical neutral species in the PECVD of the self-assembled ordered carbon nanotip arrays is shown in Fig. 2(a). The optical emission from the ICP discharge has been collected in the radial direction using a collimated optical probe mounted 6 cm below the quartz window in the diagnostic side port of the chamber. The emission is transmitted via an optical fiber to a SpectroPro-750 spectrometer (Acton Research Corporation) with the spectral resolution of 0.023 nm. The optical emission spectra of the excited neutral and ionized species have been investigated in the wavelength range 350–850 nm. Further details of the optical emission intensity (OEI) measurements can be found elsewhere.[25–27]

The optical emission spectra for the experimental conditions of Fig. 1 are shown in Fig. 2(b). Argon lines originating due to $4p \rightarrow 4s$ transition can be observed in the wavelength range 750–840 nm. Emission from the hydrogen Balmer line H_α is seen at 656.2 nm, and H_β 486.1 nm line can also be identified. Furthermore, hydrogen molecular line at 420.5 nm is present in the emission spectrum. Intense emissions from

[This article is copyrighted as indicated in the article. Reuse of AIP content is subject to the terms at: http://scitation.aip.org/termsconditions. Downloaded to] IP: 131.181.251.131 On: Mon, 14 Jul 2014 22:52:45

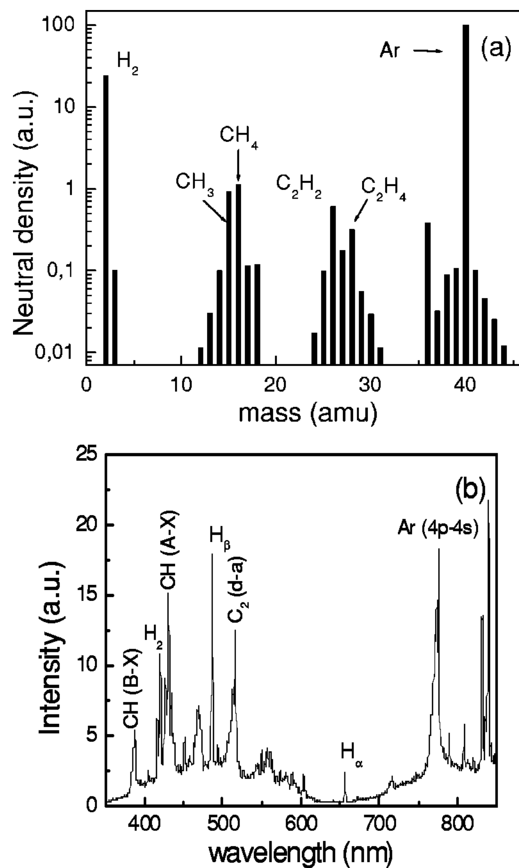

FIG. 2. Mass spectrum of the neutrals measured by QMS (a) and OES (b) of the excited species in the Ar/CH_4/H_2 plasma for the same conditions as in Fig. 1.

the active hydrocarbon and carbon species, such as the molecular bands corresponding to the $B^2\Sigma \rightarrow X^2\Pi$ and $A^2\Delta \rightarrow X^2\Pi$ transitions (at 387.1 and 431.4 nm, respectively) are also observed. The line belonging to C_2 Swan band system, corresponding to the $d^3\Pi_g \rightarrow a^3\Pi_u$ transition with $\Delta v = 0$ is located at 516.5 nm.

Due to the limited space of this article, the experimental results showing how the external parameters (rf power and gas inlet) affect the internal discharge properties (densities of neutral species and OEIs of the excited neutral species) will be presented together with the computation results to enable a direct comparison.

III. GLOBAL DISCHARGE MODEL

A. Basic assumptions

A spatially averaged (global) model has been developed to calculate the charged and neutral particle densities in the ICPs of Ar/CH_4/H_2 gas mixtures used in the PECVD of ordered carbon nanostructures. The two basic sets of equations of the model include the rf power and species balance equations. Below, we specify the basic assumptions. Table I details the neutral (seven nonradical and five radical) and charged (electrons and ten cations) species included in the computation. Anions are not accounted for here due to pronounced electropositive features of CH_4 and H_2 plasmas.[31,32]

TABLE I. Ion and neutral species in computations.

Nonradical neutrals	Ions	Radical neutrals
Ar, H_2, CH_4, C_2H_2, C_2H_4, C_2H_6, C_3H_8	H^+, H_2^+, H_3^+, CH_3^+, CH_4^+, CH_5^+, $C_2H_2^+$, $C_2H_4^+$, $C_2H_5^+$, Ar^+	H, CH, CH_2, CH_3, C_2H_5

The electron energy distribution function (EEDF) $f(\epsilon)$ is assumed Druyvesteyn-like. This assumption is supported by numerous previous studies of argon and CH_4-based rf plasmas.[33,31] Specifically,[34,35]

$$f(\epsilon) = c_1 \epsilon^{1/2} \exp(-c_2 \epsilon^x), \tag{1}$$

where $x=1$ and $x=2$ correspond to Maxwellian and Druyvesteyn EEDFs, respectively, ϵ is the electron energy, $c_1 = (x/\langle\epsilon\rangle^{3/2})[\Gamma(\xi_2)]^{3/2}/[\Gamma(\xi_1)]^{5/2}$, $c_2 = \langle\epsilon\rangle^{-x}[\Gamma(\xi_2)/\Gamma(\xi_1)]^x$, $\xi_1 = 3/2x$, and $\xi_2 = 5/2x$. The overall charge neutrality

$$\sum_i n_i = n_e \tag{2}$$

is implied, where n_e and n_i are the number densities of the electrons and cation species i, respectively. Furthermore, the temperatures of the ions and neutrals are fixed at 500 K, which is a typical gas temperature in argon-based ICP discharges[36,37] under conditions similar to the PECVD growth of ordered carbon nanostructures.[10,15]

B. Balance of radical and nonradical neutrals

The set of balance equations for methane

$$\frac{\partial n_{CH_4}}{\partial t} = I_{CH_4} - O_{CH_4} - \sum_i k_i n_e n_{CH_4} + \sum_{jkm} k_j n_k n_m - \sum_{ls} k_l n_s n_{CH_4} \tag{3}$$

and hydrogen source gases

$$\frac{\partial n_{H_2}}{\partial t} = I_{H_2} - O_{H_2} - \sum_i k_i n_e n_{H_2} + \sum_{jkm} k_j n_k n_m - \sum_{ls} k_l n_s n_{H_2} + 0.5 K_{wall}^{H} n_H \tag{4}$$

is complemented by the balance equations of other radical and nonradical neutral species

$$\frac{\partial n_r}{\partial t} = \sum_h k_h n_e n_h + \sum_{jkm} k_j n_k n_m - \sum_{ls} k_l n_s n_r - K_{wall}^{r} n_r - O_r, \tag{5}$$

where I_{CH_4}, I_{H_2} are the inflow, and O_{CH_4}, O_{H_2}, and O_r are the outflows of the CH_4, H_2, and other radical and nonradical neutral species r per unit time, respectively. A rate at which species α = Ar, CH_4, and H_2 enter the reactor $I_\alpha[\mathrm{cm^{-3}/s}] \approx 4.4 \times 10^{17} J_\alpha[\mathrm{sccm}]/V$ is proportional to the

[This article is copyrighted as indicated in the article. Reuse of AIP content is subject to the terms at: http://scitation.aip.org/termsconditions. Downloaded to] IP: 131.181.251.131 On: Mon, 14 Jul 2014 22:52:45

gas inlet flow rate J_α, where V is the chamber volume in cm^3. The rate at which the molecules leave the discharge is $O_\alpha = v_{pump} n_\alpha / V$, where v_{pump} is the pumping rate in cm^3/s. The third terms on the right-hand side of Eqs. (3) and (4) account for the losses in the electron impact reactions, whereas the fourth and fifth terms account for the gain and losses from the neutral/ion-neutral reactions, respectively. The last term in Eq. (4) reflects the fact that the atomic hydrogen is usually converted into the molecular state as a result of the surface reactions. The first term on the right-hand side of Eq. (5) describes the generation of species r as a result of the electron-impact reactions, while the second and third terms account for the gain and losses of the same species in the neutral/ion-neutral reactions, respectively. Here, $K^r_{wall} n_r$ is the number of radical neutral species r lost on the discharge walls per unit time per unit volume, where $K^r_{wall} = \gamma_r v_{thr} S_{surf}/4V$. Furthermore, γ_r and v_{thr} are the model wall sticking coefficient and the average thermal velocity of radical species r, respectively, and S_{surf} is the chamber surface area. It is further assumed that the sticking coefficients for CH, CH_2, CH_3, C_2H_5, and H species are 0.025, 0.025,[38] 0.01,[39,40] 0.01,[41,42] and 0.001,[31] respectively. The sticking probabilities of all nonradical neutral species have been assumed to be zero. Since the argon density n_{Ar} is almost invariable in the plasma reactions and is also much higher than the combined ion density, it is reasonable to assert $I_{Ar} = O_{Ar} = v_{pump} n_{Ar}/V$.

C. Plasma model

The balance equation for the cation species i is[43]

$$V n_e \nu_{iz,i} = (h_L A_L + h_R A_R) n_i u_{B,i} + V \sum_{j=1}^{N_s} k_{cx,ij} n_i n_j, \quad (6)$$

where $k_{cx,ij}$ is the charge-exchange rate coefficient for asymmetric collisions between the ion species i and neutral species j, N_s is the number of neutrals that take part in the charge-exchange collisions with the ion species i, $\nu_{iz,i}$ is the ionization frequency for the production of the ion species i. Here, $A_L = 2\pi R^2$, $A_R = 2\pi RL$, h_L and h_R are the ratios of the densities of the cation species i on the outer surfaces of a cylindrical plasma column in the axial $(z=0,L)$ and radial $(r=R)$ directions to the bulk averaged density n_i, respectively. In the low to intermediate pressure regime $[(R,L) \geqslant \lambda_i \geqslant (T_i/T_e)(R,L)]$ the above ratios are[44] $h_L = 0.86\{3 + L/2\lambda_i\}^{-1/2}$, and $h_R = 0.8\{4 + R/\lambda_i\}^{-1/2}$, where λ_i is the ion-neutral mean free path. For the EEDF Eq. (1), the velocity of ion species i at the plasma-sheath edge entering Eq. (6) is $u_{B,i} = \sqrt{2\langle\epsilon\rangle/m_i}\Gamma(\xi_1)/\sqrt{\Gamma(\xi_2)\Gamma(\xi_3)}$, where $\langle\epsilon\rangle = 1.5 T_{eff} = c_1 \int_0^\infty \epsilon^{3/2} \exp(-c_2 \epsilon^x) d\epsilon$, $\xi_3 = 1/2x$ and T_{eff} is the effective electron temperature.

The power balance equation[43]

$$P_{in} = P_{ev} + P_w \quad (7)$$

completes the basic set of Eqs. (2)–(6), where P_{in} is the total rf power deposited to the plasma. The energy lost to the electron-neutral collision processes is

$$P_{ev} = e n_e V \sum_{i=1}^{q} \nu_{iz,i} \epsilon_{L,i},$$

where q is the number of cation species generated in the discharge, and

$$\nu_{iz,i} \epsilon_{L,i} = \nu_{iz,i} \epsilon_{iz,i} + \sum_{k=1}^{N_{exc}} \nu_{exc,k} \epsilon_{exc,k} + 3 \nu_{elas} m_e T_{eff}/M_i.$$

Here, $\nu = \langle \sigma v \rangle n_n$ is the collision frequency, $\langle \sigma v \rangle$ is the rate coefficient obtained by the averaging of collision cross-section σ over the EEDF, n_n is the density of neutrals, N_{exc} is the number of excitation energy-loss channels, m_e and M_i are the electron mass and mass of ith ion, respectively. Furthermore, $\epsilon_{iz,i}$ is the threshold ionization energy for the production of the cation species i, $\nu_{exc,k}$ and $\epsilon_{exc,k}$ are the excitation frequency and threshold energy for the kth level of a neutral, $\epsilon_{L,i}$ is the total collisional energy loss for the creation of the electron-ion (species i) pair. The sum over k includes all inelastic electron-neutral collisional processes that do not produce positive ions.

In addition, a number of rotational, vibrational/electronic excitation, and dissociation processes have been taken into account here (see the Appendix and Table II). The second term in Eq. (7)

TABLE II. Electron reactions with atoms and molecules.

Reaction	Chemical reaction	Ref.
Ar, excitation	$e^- + Ar \rightarrow Ar^* + e^-$	52
Ar, ionization	$e^- + Ar \rightarrow Ar^+ + e^-$	52
CH_4, excitation	$e^- + CH_4 \rightarrow CH_4^* + e^-$ (2 vib)	53
CH_4, ionization	$e^- + CH_4 \rightarrow CH_4^+ + 2e^-$	53, 52
CH_4, ionization	$e^- + CH_4 \rightarrow CH_3^+ + H + 2e^-$	53
CH_4, dissociation	$e^- + CH_4 \rightarrow CH_3 + H + e^-$	56
CH_4, dissociation	$e^- + CH_4 \rightarrow CH_2 + 2H + e^-$	56
H, ionization	$e^- + H \rightarrow H^+ + e^-$	57
H, excitation	$e^- + H \rightarrow H^* + e^-$	55
H_2, excitation	$e^- + H_2 \rightarrow H_2^* + e^-$ (2 rot, 3 vib)	52
H_2, ionization	$e^- + H_2 \rightarrow H_2^+ + 2e^-$	57
H_2, dissociation	$e^- + H_2 \rightarrow 2H + e^-$	58
C_2H_4, excitation	$e^- + C_2H_4 \rightarrow C_2H_4^* + e^-$ (2 vib)	52, 54
C_2H_4, ionization	$e^- + C_2H_4 \rightarrow C_2H_4^+ + 2e^-$	52, 54
C_2H_4, dissociation	$e^- + C_2H_4 \rightarrow C_2H_2 + 2H + e^-$	59
C_2H_2, excitation	$e^- + C_2H_2 \rightarrow C_2H_2^* + e^-$ (3 vib)	52, 54
C_2H_2, ionization	$e^- + C_2H_2 \rightarrow C_2H_2^+ + 2e^-$	59
C_2H_6, ionization	$e^- + C_2H_6 \rightarrow C_2H_6^+ + 2e^-$	59
C_2H_6, ionization	$e^- + C_2H_6 \rightarrow C_2H_5^+ + H + 2e^-$	59
C_2H_6, dissociation	$e^- + C_2H_6 \rightarrow C_2H_5 + H + e^-$	59
C_2H_6, dissociation	$e^- + C_2H_6 \rightarrow C_2H_4 + 2H + e^-$	59
C_2H_5, ionization	$e^- + C_2H_5 \rightarrow C_2H_5^+ + 2e^-$	59
C_2H_5, ionization	$e^- + C_2H_5 \rightarrow C_2H_4^+ + H + 2e^-$	59
C_2H_5, dissociation	$e^- + C_2H_5 \rightarrow C_2H_4 + H + e^-$	59
CH_2, ionization	$e^- + CH_2 \rightarrow CH_2^+ + 2e^-$	59
CH_2, dissociation	$e^- + CH_2 \rightarrow CH + H + e^-$	59
CH_3, ionization	$e^- + CH_3 \rightarrow CH_3^+ + 2e^-$	59
CH_3, dissociation	$e^- + CH_3 \rightarrow CH_2 + H + e^-$	59
CH_3, dissociation	$e^- + CH_3 \rightarrow CH + 2H + e^-$	59

[This article is copyrighted as indicated in the article. Reuse of AIP content is subject to the terms at: http://scitation.aip.org/termsconditions. Downloaded to] IP: 131.181.251.131 On: Mon, 14 Jul 2014 22:52:45

TABLE III. Neutral-neutral reactions.

Reaction	Rate constant k (cm^3 s^{-1})	Ref.
$H+CH_4 \rightarrow CH_3+H_2$	$2.2\times10^{-20}T_g^3 \exp(-4045/T_g)$	60
$H+CH_3 \rightarrow CH_2+H_2$	$1\times10^{-10} \exp(-7600/T_g)$	60
$H+CH_2 \rightarrow CH+H_2$	$1\times10^{-11} \exp(900/T_g)$	60
$H+C_2H_6 \rightarrow C_2H_5+H_2$	$2.4\times10^{-15}T_g^{1.5} \exp(-3730/T_g)$	60
$H+C_2H_5 \rightarrow 2CH_3$	6×10^{-11}	60, 61
$H+C_2H_5 \rightarrow C_2H_4+H_2$	5×10^{-11}	60
$H+C_2H_4 \rightarrow C_2H_3+H_2$	$9\times10^{-10} \exp(-7500/T_g)$	60
$H+C_2H_2 \rightarrow C_2H+H_2$	$1\times10^{-10} \exp(-14\,000/T_g)$	60
$CH_3+CH_3 \rightarrow C_2H_6$	6×10^{-11}	60
$CH_3+CH_3 \rightarrow C_2H_5+H$	$5\times10^{-11} \exp(-6800/T_g)$	60
$CH_3+CH_3 \rightarrow C_2H_4+H_2$	$1.7\times10^{-8} \exp(-16\,000/T_g)$	60
$CH_3+CH_2 \rightarrow C_2H_4+H$	7×10^{-11}	60
$CH_3+CH \rightarrow C_2H_3+H$	5×10^{-11}	60
$CH_2+CH_2 \rightarrow C_2H_4$	1.7×10^{-12}	60
$CH_2+CH_2 \rightarrow C_2H_2+H_2$	$2\times10^{-10} \exp(-400/T_g)$	60
$CH+CH_4 \rightarrow C_2H_4+H$	1×10^{-10}	60
$CH+CH_2 \rightarrow C_2H_2+H$	6.6×10^{-11}	60
$CH+CH \rightarrow C_2H_2$	2×10^{-10}	60
$C_2H_5+CH_3 \rightarrow C_3H_8$	4.2×10^{-12}	20
$CH+C_2H_6 \rightarrow C_3H_8$	4×10^{-10}	19

TABLE IV. Ion-neutral reactions.

Reaction	k (cm^3 s^{-1})	Ref.
$CH_4^+ + CH_4 \rightarrow CH_5^+ + CH_3$	1.5×10^{-9}	61
$CH_4^+ + H_2 \rightarrow CH_5^+ + H$	3.3×10^{-11}	61
$CH_3^+ + CH_4 \rightarrow CH_4^+ + CH_3$	1.36×10^{-10}	61
$Ar^+ + H_2 \rightarrow ArH^+ + H$	1.6×10^{-9}	62
$Ar^+ + H_2 \rightarrow Ar + H_2^+$	2.7×10^{-10}	62
$Ar^+ + CH_4 \rightarrow CH_3^+ + H + Ar$	1.05×10^{-9}	63
$H_2^+ + H_2 \rightarrow H + H_3^+$	2.5×10^{-9}	61
$CH_3^+ + CH_4 \rightarrow C_2H_5^+ + H_2$	1.2×10^{-9}	61
$H_3^+ + C_2H_6 \rightarrow C_2H_5^+ + 2H_2$	2.0×10^{-9}	18
$H_3^+ + CH_4 \rightarrow CH_5^+ + H_2$	1.6×10^{-9}	61
$H_3^+ + C_2H_4 \rightarrow C_2H_5^+ + H_2$	1.9×10^{-9}	61
$H_3^+ + C_2H_2 \rightarrow C_2H_3^+ + H_2$	1.94×10^{-9}	61
$C_2H_2^+ + CH_4 \rightarrow C_2H_3^+ + CH_3$	4.1×10^{-9}	61
$C_2H_2^+ + CH_4 \rightarrow C_3H_4^+ + H_2$	6.25×10^{-10}	61
$C_2H_2^+ + CH_4 \rightarrow C_3H_5^+ + H$	1.44×10^{-9}	61
$C_2H_4^+ + C_2H_4 \rightarrow C_3H_5^+ + CH_3$	3.9×10^{-10}	61
$C_2H_4^+ + C_2H_4 \rightarrow C_4H_8^+$	4.3×10^{-10}	61
$CH_5^+ + C_2H_6 \rightarrow C_2H_5^+ + H_2 + CH_4$	5.0×10^{-10}	18
$C_2H_4^+ + C_2H_6 \rightarrow C_3H_6^+ + CH_4$	2.03×10^{-13}	61
$C_2H_4^+ + C_2H_6 \rightarrow C_3H_7^+ + CH_3$	1.32×10^{-11}	61
$C_2H_5^+ + C_2H_2 \rightarrow C_4H_7^+$	6.7×10^{-10}	61
$C_2H_5^+ + C_2H_4 \rightarrow C_3H_5^+ + CH_4$	3.1×10^{-10}	61
$C_2H_5^+ + C_2H_4 \rightarrow C_4H_9^+$	3.0×10^{-10}	61

$$P_w = \sum_{i=1}^{g} e n_i v_{B,i}(h_L A_L + h_R A_R)(\epsilon_{e\omega} + \epsilon_{i\omega})$$

stands for the loss of kinetic energy of charged species to the discharge walls. The mean electron kinetic energy lost per electron lost to the walls is[35] $\epsilon_{ew} = \langle\epsilon\rangle\Gamma(\xi_1)\Gamma(\xi_5)/(\Gamma(\xi_2)\Gamma(\xi_4))$, where $\xi_4 = 2/x$ and $\xi_5 = 3/x$. The ion kinetic energy lost per ion lost to the wall ϵ_{iw} is the sum of the ion energy at the sheath edge and the energy gained by the ion as it traverses the sheath[35] $\epsilon_i = \langle\epsilon\rangle\Gamma(\xi_1)^2/(\Gamma(\xi_2)\Gamma(\xi_3)) + V_s$, where V_s is the sheath voltage drop. For argon ions and Maxwellian EEDF, $V_s \approx 4.68 T_{\mathrm{eff}}$; for Druyvesteyn distribution $V_s \approx 3.43 T_{\mathrm{eff}}$.[35] Description of the numerical method for the solution of the global model Eqs. (3)–(7), the chemical reactions used in the computation, and the rate coefficients for the reactions are presented in the Appendix and Tables II–IV.

IV. DENSITIES OF NEUTRAL AND CHARGED SPECIES

The global model of the previous section is used here to investigate the effect of the discharge operating conditions on the main plasma parameters, including the number densities of the neutrals, electrons and ions, as well as the electron temperature. The discharge parameters are computed for different powers P_{in} absorbed in the discharge, and the input flow rates of argon and methane. The computation results are compared with the QMS experimental data and are used to explain the variations of the OEI of selected CH (431.4 nm), C_2 (516.5 nm), hydrogen (656.2 nm) and argon (839.8 nm) emission lines.

A. Effect of rf power

We now consider the effect of the input power on the densities of the major discharge species. The methane, hydrogen and argon input flow rates are fixed at 7.5, 12.4, and 35 sccm, respectively, which corresponds to $n_{CH_4} = 1.37 \times 10^{14}$ cm^{-3}, $n_{H_2} = 2.27\times10^{14}$ cm^{-3}, and $n_{Ar} = 6.4 \times 10^{14}$ cm^{-3} under the "plasma-off" conditions, respectively. To study the effect of rf power on the plasma parameters, P_{in} is varied in the numerics in the range from 50 W to 3 kW, which is broader than was actually used in the PECVD of CNs (1.8–3.0 kW).[10,15]

Figure 3(a) shows the calculated densities of nonradical and radical neutrals in the $Ar/CH_4/H_2$ discharge of interest here. The variations of the electron and ion densities on P_{in} are shown in Fig. 3(b). It is seen from Fig. 3(a) that both n_{CH_4} and n_{H_2} drop dramatically with P_{in}. We note that in the power range of the CN growth, methane and hydrogen densities in the plasma are much smaller than in the absence of the discharge. Meanwhile, Ar atoms appear to be the dominant neutral species in the discharge. The density of hydrogen atoms is approximately 25 times smaller than the argon density and slightly decreases with power. As can be seen in Fig. 3(a), the density of molecular hydrogen at low input powers is comparable to that of atomic hydrogen, and also diminishes with P_{in}. The latter decrease can be attributed to the enhanced dissociation of hydrogen molecules at higher input powers accompanied by the rise in the electron number density [Fig. 3(b)]. Under the CN growth conditions, the hydrogen conversion factor[18] (degree of dissociation) can approach 99%. The enhanced H_2 dissociation is naturally accompanied by the rise of the ratio of the densities of H and H_2 species, which can exceed 10 at elevated powers. Similar high n_H/n_{H_2} ratios have previously been reported by Bera, Farouk, and Vitello.[22]

Likewise, the densities of methane and CH_3, C_2H_2, C_2H_4, C_2H_5, C_2H_6, and C_3H_8 species also decrease with rf power, which can be due to more intense electron-neutral

[This article is copyrighted as indicated in the article. Reuse of AIP content is subject to the terms at: http://scitation.aip.org/termsconditions. Downloaded to] IP: 131.181.251.131 On: Mon, 14 Jul 2014 22:52:45

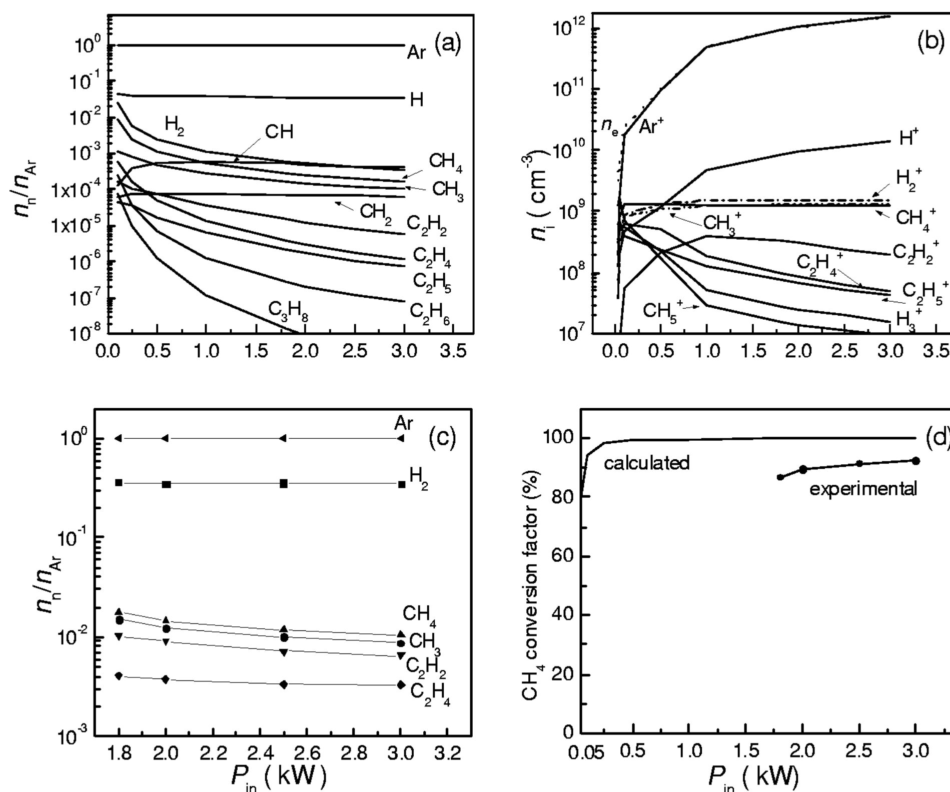

FIG. 3. Computed (a) and QMS measured (c) densities of neutrals (normalized on n_{Ar}), computed ion densities (b), and computed and QMS measured CH_4 conversion factor ϖ_{CH_4} (d) as functions of the power input for the same gas feedstock as in Fig. 1.

collisions at higher electron densities. On the other hand, CH and CH_2 densities increase with P_{in}. The latter can be attributed to the smaller sizes of CH and CH_2 molecules relative to other hydrocarbon species. A similar tendency has previously been reported elsewhere.[19] Therefore, it is probable that the above two molecules do not react with the plasma species as intensively as CH_3, C_2H_2, C_2H_4, C_2H_5, C_2H_6, and C_3H_8 species. Hence, higher hydrocarbons C_xH_y ($x \geqslant 2$) are more likely to break up into smaller radical fragments. This could be a reason why the densities of C_2H_6 and C_3H_8 are quite low. However, the relative importance of the above two (as well as C_2H_5) species is higher at lower input powers, as can be seen in Fig. 3(a).

The results of the QMS measurements in Fig. 3(c) confirm that the densities of H_2, CH_4, CH_3, C_2H_2, and C_2H_4 species drop with rf power. Similarly, the CH_4 conversion factor $\varpi_{\mathrm{CH}_4} = 1 - n_{\mathrm{CH}_4}/n^0_{\mathrm{CH}_4}$, where $n^0_{\mathrm{CH}_4}$ is the CH_4 density under the plasma-off conditions, appears to be very high at input powers exceeding 1.8 kW.

A comparison between the experimental and calculated values of ϖ_{CH_4} at variable rf power in Fig. 3(d) shows a consistent tendency of ϖ_{CH_4} to rise with power, giving a remarkable quantitative agreement between the computation and the experiment. In the power range for the CN growth (1.8–3 kW), the conversion factor measured by the QMS varies from 86% to 92%, whereas the numerical value of ϖ_{CH_4} remains approximately 99%. Similar high degrees of the methane dissociation ($\sim$95%) in CH_4/H_2 inductively coupled plasmas have previously been reported.[24] High conversion rates of hydrogen-diluted reactive gas feedstocks is a common feature of many chemically active plasmas. For example, ϖ_{SiH_4} can be as high as 99% in SiH_4/H_2 gas mixtures.[45] Apparently large conversion factors are due to the higher abundance of atomic hydrogen at elevated electron densities in hydrogen-containing plasmas, which in turn results in more intense chemical reactions between H and CH_4 (or SiH_4 in silane plasmas).

The optical emission intensities of neutral CH (431.4 nm), C_2 (516.5 nm), hydrogen (660.2 nm) and argon (839.8 nm) lines have also been studied under variable rf power conditions. The OEIs of the above spectral lines *versus* rf power are shown in Fig. 4(a). One can see that the intensities of the lines grow with P_{in}. The rise can be explained by noting that the OEIs of excited neutral species are proportional to the densities of the plasma electrons n_e and the corresponding neutral species n_α, and also depend on the effective electron temperature.[33,46] As the global model suggests, T_{eff} is almost invariant as the input power increases ($\approx$3.5 eV in the power range considered). The OEI is thus proportional to the product $n_e n_\alpha$. In Fig. 4(b), the normalized dependencies of the OEI on P_{in} are compared with the calculated $n_e n_\alpha$ for neutral argon (839.8 nm), CH (431.4 nm) and hydrogen (656.2 nm) emission lines. One can see that the variation of the product of n_e and n_α with rf power is very similar to that of the OEIs. Moreover, since in the power range of 1.8–3.0 kW the density variation of the neutral species with power is quite small, the OEI rise with P_{in} can be attributed to the higher electron densities. In this cal-

[This article is copyrighted as indicated in the article. Reuse of AIP content is subject to the terms at: http://scitation.aip.org/termsconditions. Downloaded to] IP: 131.181.251.131 On: Mon, 14 Jul 2014 22:52:45

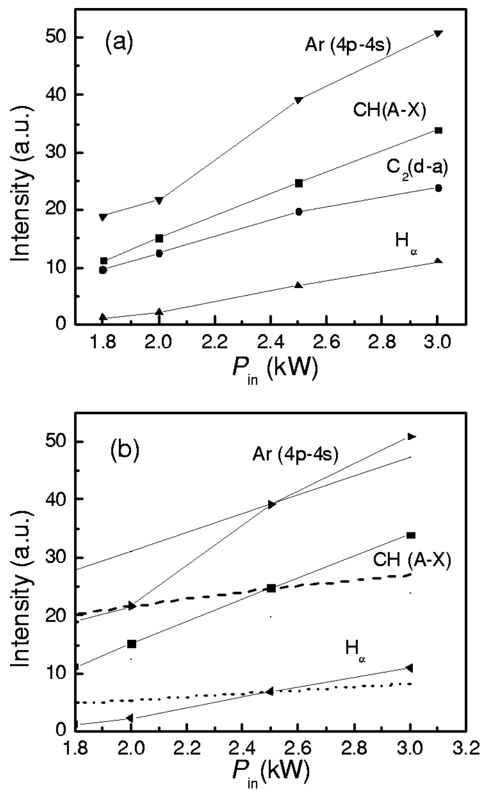

FIG. 4. Measured OEIs of CH (431.4 nm), C_2 (516.5 nm), H (656.2 nm) and Ar (839.8 nm) lines vs P_{in} (a). The OEIs are compared with the product $n_e n_\alpha$ (b), where α=Ar (solid line), CH (dashed line) and H (dotted line).

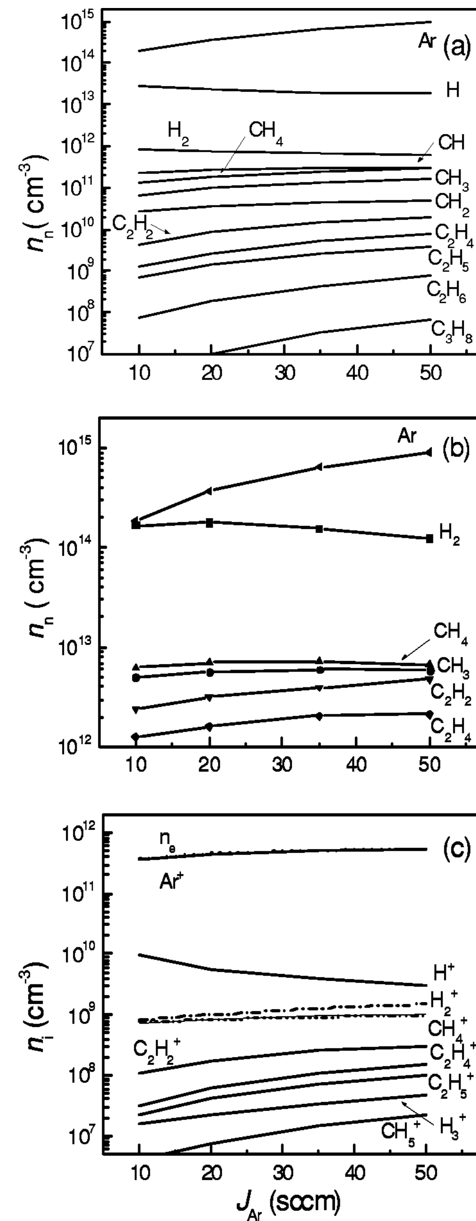

FIG. 5. The computed (a) and QMS measured (b) densities of neutrals and computed densities of charged particles (c) as functions of J_{Ar} for J_{CH_4} $=6.0$ sccm, $J_{H_2}=12.4$ sccm, and $P_{in}=2$ kW.

culation, P_{in} denotes the actual rf power deposited to the plasma, which critically depends on the system setup.[47]

B. Effect of argon dilution

To study the effect of the input Ar flow rate J_{Ar} on the densities of the abundant discharge species, we increase J_{Ar} from 10 to 50 sccm and keep the flow rates of methane and hydrogen ($J_{CH_4}=6.0$ sccm, $J_{H_2}=12.4$ sccm), as well as the input power ($P_{in}=2$ kW) fixed. These input parameters are typical in the PECVD of carbon nanostructures.[10,15] Figure 5(a) displays the variation of the densities of radical/nonradical neutral species with the argon inflow rate. One can see that the densities of molecular and atomic hydrogen decrease with Ar inlet, whereas the densities of hydrocarbon neutrals grow with J_{Ar}. The results of the QMS measurements shown in Fig. 5(b) support the computed trends for the densities of H_2, CH_4, CH_3, C_2H_2, and C_2H_4 species. The decline of the molecular and atomic hydrogen species can be due to the variation of the electron density [Fig. 5(c)] and effective temperature (T_{eff}=4.27, 3.87, 3.6, and 3.45 eV for J_{Ar}= 10,20,35, and 50 sccm, respectively) with J_{Ar}. Hence, the methane conversion in collisional processes weakens, and, as a consequence, densities of CH_4 and other carbon-bearing species increase.

We have also examined the variation of the intensities of the selected spectral lines with argon inlet. Figure 6(a) shows the dependencies of the OEIs of CH, C_2, hydrogen, and argon lines on the Ar input flux. The results of the comparison of the variations of the product $n_e n_\alpha$ and the OEIs of Ar (839.8 nm) and CH (431.4 nm) lines with J_{Ar} are displayed in Fig. 6(b). It is seen that the intensities of the selected lines grow with the argon density. However, the OEI of the argon line grows slower than the product of n_e and n_{Ar}. On the contrary, the OEI of CH line grows faster than $n_e n_{CH}$. The discrepancies between the variation of the OEI and $n_e n_\alpha$ with J_{Ar} can be due to remarkable changes in T_{eff} as well as numerous complex elementary processes, including stepwise excitations.

C. Effect of methane inlet

Here, the effect of the input methane flux on the discharge parameters is studied. Figure 7(a) shows the dependence of the densities of the neutral species on J_{CH_4}. A higher inflow of CH_4 is naturally accompanied by the rise of

[This article is copyrighted as indicated in the article. Reuse of AIP content is subject to the terms at: http://scitation.aip.org/termsconditions. Downloaded to] IP: 131.181.251.131 On: Mon, 14 Jul 2014 22:52:45

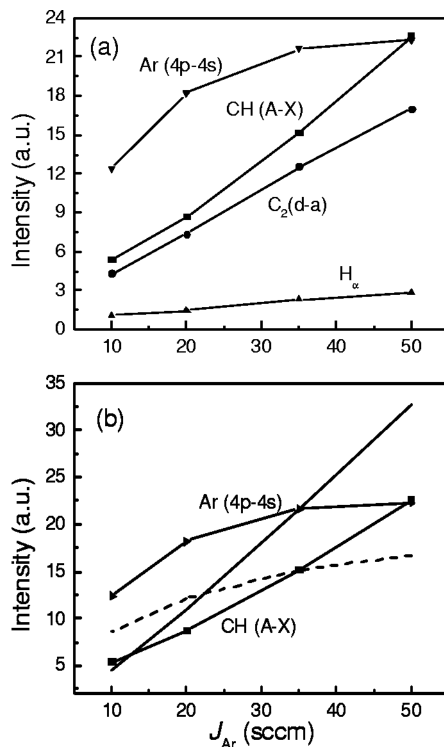

FIG. 6. Same as in Fig. 4(a) as a function of J_{Ar} (a). The OEIs for Ar and CH lines compared with the product $n_e n_\alpha$ (b), where α= Ar (solid line) and CH (dash line). Conditions are the same as in Fig. 5.

the densities of methane and most of the hydrocarbon neutrals. An increase of the atomic hydrogen density can be due to the enhancement of the electron-impact dissociation of CH_4 (Table II). On the other hand, more molecular hydrogen is released as a result of the intensified heavy particle collisions (Table III). The QMS measurements also confirm that the densities of H_2, CH_4, CH_3, C_2H_2, and C_2H_4 species grow with the input methane flux [Fig. 7(b)]. The computed variations of the electron and ion number densities with J_{CH_4} are shown in Fig. 7(c). It is seen that the electron density slightly decreases, which can be attributed to higher inelastic energy losses in inelastic electron-neutral collisions (e.g., for the vibrational, rotational, and electronic excitations of hydrogen and hydrocarbon species) that inevitably accompany a higher inlet of CH_4.

The changes in the densities of neutral [Fig. 7(a)] and charged [Fig. 7(c)] species with J_{CH_4} have been used for the analysis of the corresponding variations of the OEIs shown in Fig. 7(d). It is clearly seen that the emission intensities fall when more methane is inlet in the plasma reactor. Presumably, this drop is mainly due to a decline of the electron density with J_{CH_4}.

V. DEPOSITED NEUTRAL AND ION FLUXES

In this section we study the fluxes of the neutral and charged species deposited onto the substrate under the CN growth conditions. To understand the role of each species in the PECVD and to study the effect of the input plasma parameters on the deposition process, we compare the numbers

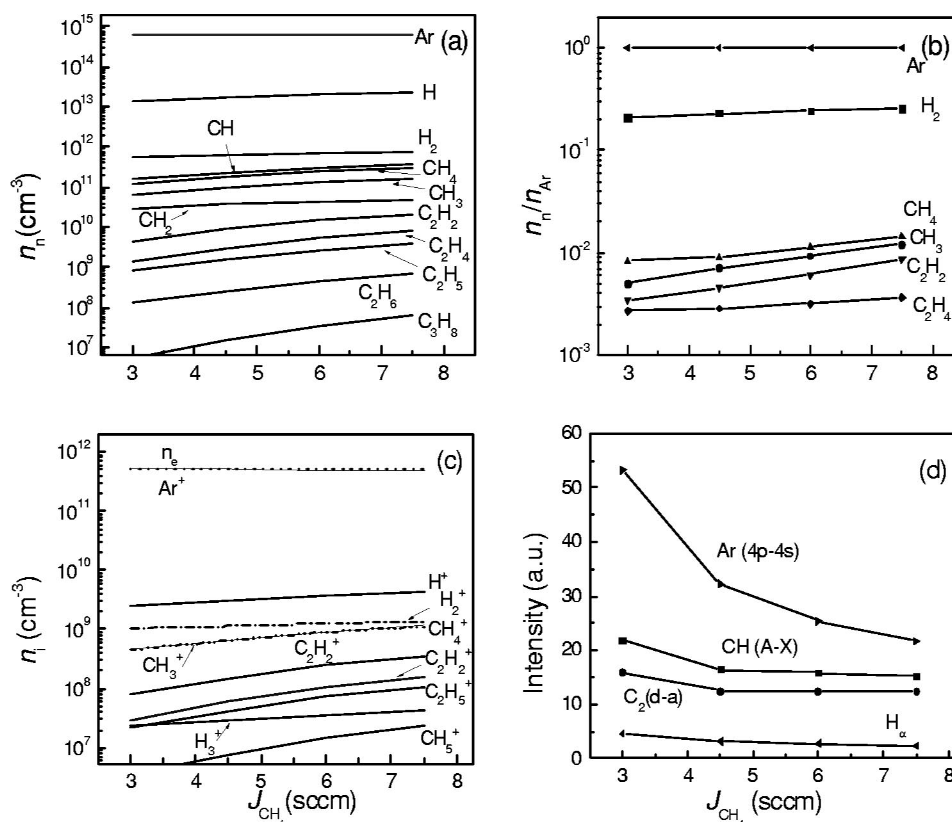

FIG. 7. The calculated (a) and QMS measured (normalized on n_{Ar}) densities of neutral species (b); computed densities of charged species (c), and OEIs of the selected neutral lines (d) vs J_{CH_4} for J_{Ar}= 35 sccm, J_{H_2}= 12.4 and P_{in}= 2 kW.

[This article is copyrighted as indicated in the article. Reuse of AIP content is subject to the terms at: http://scitation.aip.org/termsconditions. Downloaded to] IP: 131.181.251.131 On: Mon, 14 Jul 2014 22:52:45

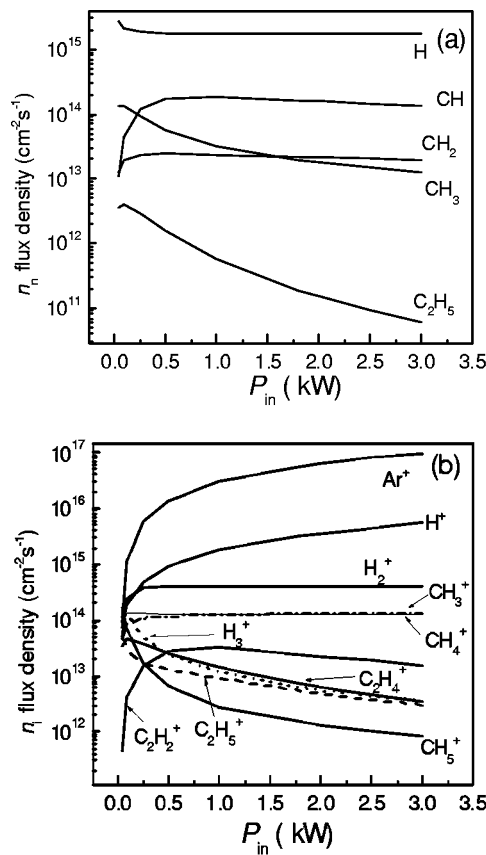

FIG. 8. Deposited flux density of radical neutrals (a) and ions (b) as a function of P_{in} for the same conditions as in Fig. 1.

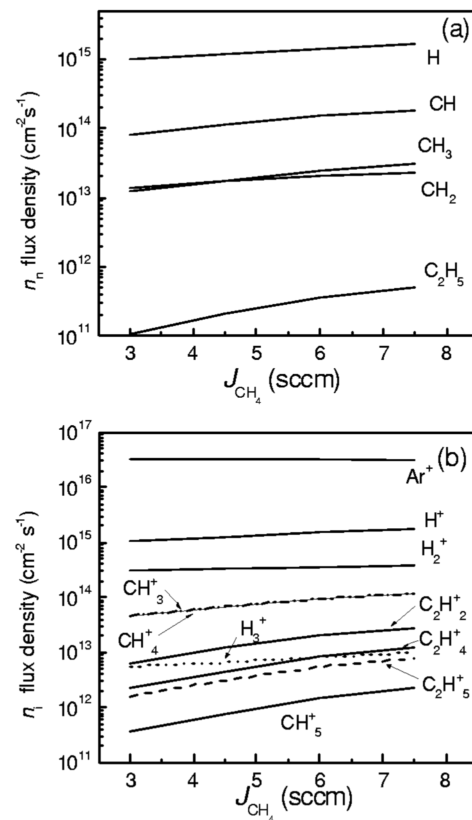

FIG. 9. Same as in Fig. 8 as a function of methane inflow rate for the same conditions as in Fig. 7.

of the radical neutrals deposited per unit time per unit surface $\Psi_n^j = 0.25 n_j \gamma_j v_{thj}$ with those of the plasma ions $\Psi_i = h_L n_i v_{Bi}$. Here and below indexes j and i denote radical and ion species, respectively. Here we recall that in our model only H, CH, CH_2, CH_3, and C_2H_5 radical neutrals are considered to be able to deposit on the film surface. Figure 8(a) illustrates the effect of the input power on the deposited fluxes of the radical neutrals. At low input powers ($P_{in} < 0.25$ kW), atomic hydrogen and methyl are the main radical neutrals deposited on the processing surface [Fig. 8(a)]. When the rf power increases to $P_{in} \sim 0.75$ kW, the flux of CH increases. Furthermore, CH appears to be the major contributor to the carbon material deposition at relatively high input powers ($\geqslant 0.5$ kW). Meanwhile, the flux of atomic hydrogen is about ten times higher than those of the carbon-bearing neutrals. This finding supports the assertion of the crucial role of the catalyzed surface etching by the atomic hydrogen in the PECVD of CNs.[48]

The dependence of the deposited ion fluxes on P_{in} is shown in Fig. 8(b). Under low input powers (~ 0.05 kW), CH_5^+ flux is dominant. With an increase of the rf power the fluxes of Ar^+ and H^+ also increase due to the rise of the corresponding ion densities. Furthermore, at relatively high powers ($\geqslant 0.4$ kW) the fluxes of Ar^+ and H^+ cations become dominant. In this case, the H^+ flux is approximately ten times smaller than that of Ar^+. Meanwhile, the fluxes of CH_4^+ and CH_3^+ are the strongest among the carbon-containing ions. However, the fluxes of CH_4^+ and CH_3^+ are in 2–3 orders of magnitude smaller than those of argon ions. Under the typical CN PECVD conditions ($P_{in} \sim 2$ kW), the deposited flux of hydrogen atoms is comparable with that of H^+ ions.

The total flux density of the hydrocarbon radical neutrals Ψ_n strongly depends on the input power. At $P_{in} = 0.05$ kW, $\Psi_n \sim 1.63 \times 10^{14}$ s^{-1} cm^{-2} and further grows to 2.55×10^{14} s^{-1} cm^{-2} at 0.5 kW. In the subsequent power range (0.5–3.0 kW) the flux density declines with power. For instance, $\Psi_n = 2.42$, 1.98, 1.62×10^{14} s^{-1} cm^{-2} at $P_{in} = 1$, 2, and 3 kW, respectively. The total flux density of hydrocarbon ions onto the processing surface Ψ_i is slightly higher than Ψ_n and drops with P_{in} in the entire power range of interest here. Specifically, $\Psi_i = 3.66$, 3.14, 3.02, 2.85, 2.75 $\times 10^{14}$ s^{-1} cm^{-2} at $P_{in} = 0.05$, 0.5, 1, 2, and 3 kW, respectively. We have further revealed that under the prevailing carbon nanotip growth conditions ($P_{in} = 2-3$ kW) Ψ_i is ~ 1.5 times higher than Ψ_n.

The densities of radical neutral/ion fluxes onto the surface also depend on the methane inlet. The dependence of the radical neutral and ion flux densities on J_{CH_4} is shown in Figs. 9(a) and 9(b), respectively. One can conclude from Fig. 9 that the fluxes of all hydrocarbon species grow with the methane input flow rate. This can be attributed to the rise of the corresponding neutral and ion densities. The total fluxes of ions and radical neutrals are almost the same at relatively low input flow rates of CH_4. Specifically, Ψ_i and Ψ_n are 1.56 and 1.51×10^{14} s^{-1} cm^{-2} at $J_{CH_4} = 4.5$ sccm, respectively. With an increase of J_{CH_4} to 7.5 sccm, the total ion flux

[This article is copyrighted as indicated in the article. Reuse of AIP content is subject to the terms at: http://scitation.aip.org/termsconditions. Downloaded to] IP: 131.181.251.131 On: Mon, 14 Jul 2014 22:52:45

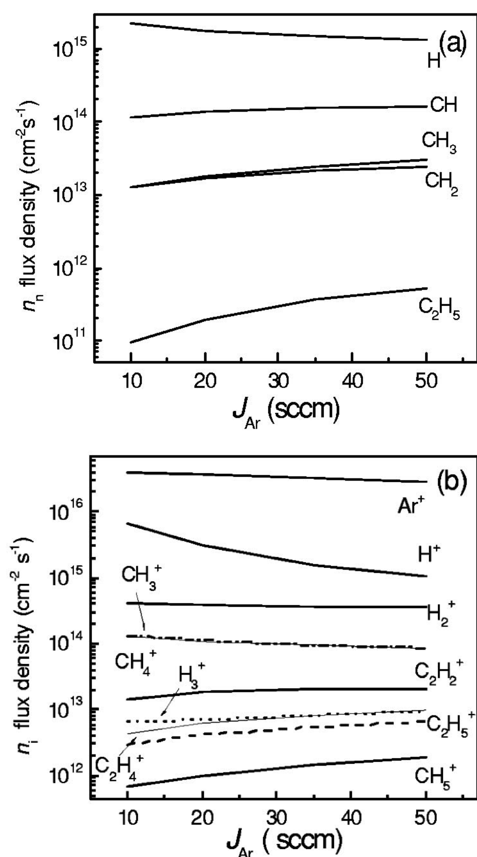

FIG. 10. Same as in Fig. 9 as a function J_{Ar} for the same conditions as in Fig. 5.

$\Psi_i = 2.85 \times 10^{14}\ s^{-1}\ cm^{-2}$ becomes approximately 20% higher than that of the radical neutrals $\Psi_n = 2.34 \times 10^{14}\ s^{-1}\ cm^{-2}$.

Variation of the argon input flow rate also affects the neutral and ion fluxes onto the processing surface. Figures 10(a) and 10(b) demonstrate how the deposited neutral and ion flux densities depend on J_{Ar}. From Fig. 10(a) it is seen that the flux densities of CH, CH_3, CH_2 and C_2H_5 radicals grow with J_{Ar}, whereas that of the atomic hydrogen slightly drops. These tendencies apparently follow the dependence of the corresponding radical densities on J_{Ar} shown in Fig. 5(a). On the other hand, the ion fluxes depend on the corresponding ion densities as well as the effective electron temperature. The ion flux dependence on J_{Ar} is thus similar to those for the ion densities. However, H_2^+, Ar^+, CH_4^+, and CH_3^+ flux densities slightly decrease with an increase of argon input flow rate, even though the H_2^+, Ar^+, CH_4^+, and CH_3^+ densities rise [Fig. 5(c)]. This presumably happens since the electron temperature declines with J_{Ar}.

Hence, the combined hydrocarbon ion flux on the processing surface also diminishes with J_{Ar} as a result of the drop in the CH_4^+ and CH_3^+ ion fluxes. Indeed, $\Psi_i = 2.81$, 2.49, $2.24 \times 10^{14}\ s^{-1}\ cm^{-2}$ at $J_{Ar} = 10$, 20, and 35 sccm, respectively. On the contrary, the total hydrocarbon neutral flux is slightly smaller than Ψ_i and rises with J_{Ar}. For example, $\Psi_n = 1.42$, 1.72, $1.97 \times 10^{14}\ s^{-1}\ cm^{-2}$ at the same argon inlet flow rates. At higher argon inlet flow rates the difference between the absolute values of the ion and neutral fluxes becomes very small.

VI. DISCUSSION AND CONCLUSION

We now discuss the main results obtained and the limitations of the model. Generally, the modeling and experimental results appear to be in good agreement, especially the variation trends of the number densities of the main neutral species H_2, CH_4, CH_3, C_2H_2, and C_2H_4 with the input power and methane/argon inlet flow rates. The global model also explains how the input parameters affect the OEIs of different emission lines in Ar/CH_4/H_2 discharges used for the PECVD of carbon nanostructures.

We have shown experimentally and numerically that methane and hydrogen conversion rates are very high ($\sim$99%). This happens because of the high electron number densities in low-frequency inductively coupled plasmas, which enhance the dissociation of molecular hydrogen and generation of large amounts of atomic hydrogen. Hydrogen atoms, in turn, further accelerate the methane dissociation. It was also shown that the ion, neutral and radical densities in the discharge can be efficiently controlled by the input power (Fig. 3) and methane/argon input flow rates (Figs. 5 and 7). The electron, Ar^+ and H^+ densities, as well as the methane conversion factor, increase with power. Meanwhile, the densities of most of hydrocarbon neutrals drop with P_{in} due to the enhancement of their collisions with the plasma electrons and ions. An increase of the input argon flow rate is accompanied by the rise of the densities of electrons, Ar^+, and hydrocarbon neutrals and cations [Figs. 5(a)–(c)]. On the contrary, the effective electron temperature and the densities of the atomic and molecular hydrogen neutrals and H^+ cations decline with J_{Ar}. The electron density growth is presumably due to the rise of argon density with respect to other neutrals, the latter also leading to the weakening of the role of rotational and vibrational molecular excitations in the discharge power balance.

We note that the averaged ion diffusion losses decrease with the argon inlet due to the enhanced production of heavy Ar^+ ions and result in somewhat lower values of the effective electron temperature. Another factor contributing to the decline of T_{eff} with extra argon inlet is a decrease of the role of ion-neutral recombination losses due to stronger, compared to Ar^+, interaction of carbon and hydrogen-containing cations with other particles. The rise of n_e and drop in T_{eff} result in the depletion of H and H_2 species.

Higher inflow of the carbon source gas CH_4 naturally enhances the generation of C_xH_y cations and radical neutrals (here $x = 1-2$ and $y = 1-6$, and 8). Thus, various inelastic collisional processes intensify, which results in somewhat lower electron number densities. Furthermore, the electron-impact reactions involving a larger number of C_xH_y neutrals (see Table II) yield larger amounts of atomic hydrogen, the latter contributing to higher densities of H_2 as a result of $C_xH_y + H$ reactions (Table III).

The results in Fig. 3(a) suggest that the densities of the neutral species C_2H_5, C_2H_6, and C_3H_8 at higher input powers are very low and the output of the simulation is affected

[This article is copyrighted as indicated in the article. Reuse of AIP content is subject to the terms at: http://scitation.aip.org/termsconditions. Downloaded to] IP: 131.181.251.131 On: Mon, 14 Jul 2014 22:52:45

very little by the inclusion of the above species in the model. To this effect, a simplified spatially averaged (global) discharge model would not need the inclusion of the above species. However, similar to the computations of Ref. 18, we did retain the above species in the computations due to the fact that higher hydrocarbons are more abundant at lower input powers as well as play an important role in the gas-phase polymerization of carbon-based nanoparticles.[49,50]

Our model also did not include the number balance of the excited species that would otherwise be able to enhance the species production through a number of stepwise processes. Indeed, the actual ion density in 1 mTorr argon discharge can be elevated up to 25% due to the contribution of the excited species.[51] However, this effect is not so strong in the pressure range considered here.[51] Nevertheless, the power lost to the rotational, vibrational, and electronic excitations is implicitly included in the power balance Eq. (7).

The computed T_{eff}, ion and radical neutral densities can be used to analyze the fluxes of different species onto the catalyzed substrate in the CN PECVD process. The numerics reveal that total hydrocarbon neutral flux Ψ_n is approximately 1.5 times smaller than the ion one Ψ_i in a typical carbon nanotip growth process with $P_{\mathrm{in}}=1.8-3.0$ kW, $J_{\mathrm{CH_4}}=7.5$ sccm, $J_{\mathrm{H_2}}=12.4$ sccm, and $J_{\mathrm{Ar}}=35$ sccm. Varying the inflow rates of argon and methane, one can control the ratio Ψ_i/Ψ_n. An increase of the argon input flow rate results in a pronounced growth of Ψ_n and diminishing of Ψ_i. At higher argon inlet, one can achieve $\Psi_i \simeq \Psi_n$. The total fluxes of the ion and neutral hydrocarbon species naturally grow with $J_{\mathrm{CH_4}}$. At low methane inlets $\Psi_i \sim \Psi_n$, whereas at higher $J_{\mathrm{CH_4}}$ the deposited flux of hydrocarbon cations can be $\sim 20\%$ higher than the neutral flux. Therefore, the ion fluxes onto the nanostructured surface in the CN growth process can exceed those of the neutral species and thus play a crucial role in the growth of nanonostructured carbon-based films.

We note that some quantitative discrepancies between the computed and QMS measured densities of the neutral species still remain. It is thus worthwhile to discuss the reasons for the difference, namely, the limitations of the global model and the accuracy of the QMS measurements. A direct comparison of the experimental and numerical results in Figs. 3(a) and 3(c) shows that the QMS data on the normalized densities of the major species are consistently higher than the computed values. This discrepancy can be due to lower, than the spatially averaged (considered in the model), electron densities and CH_4/H_2 dissociation rates at the connection point (5 cm below the quartz window) of the reactor chamber with the QMS device.[33]

Meanwhile, the QMS measurements reveal very small densities of CH and CH_2 radical neutrals [see Fig. 2(a)]. It could happen because of their deposition onto the inner surfaces of relatively long (25 cm) and thin (3 cm internal diameter) vacuum-tight bellows connecting the reactor and QMS chambers. The precision of the QMS measurements can certainly be improved by shortening the connection bellows. However, this can affect the quality of the deposition process, where radical neutrals play a pivotal role. We thus limited ourselves by the qualitative analysis of the mass spectra of the discharge species and their variations with the external parameters, which were found in a remarkable agreement with the computation results. Another reason for the discrepancy between the QMS measured and computed densities of the neutral species is that the global model actually provides only the averaged number densities of the species.

Finally, a two-dimensional model has to be developed to include the effects of the nonuniformity in real PECVD processes. Our model can also be improved by involving the major chemical reactions on the nanostructured carbonaceous surfaces. This and some other points will be a worthwhile attempt in the near future.

ACKNOWLEDGMENTS

This work was supported by the Agency for Science, Technology, and Research of Singapore (Project No. 012-101-0024) and the Australian Research Council. Assistance of Z. L. Tsakadze in the OES and QMS measurements and the interpretation of the results is kindly appreciated. K. O. thanks M. Meyyappan, D. Hash, J. Roepcke, and B. Cruden for their stimulating comments.

APPENDIX

Rate coefficients for electron-neutral collisions in Eqs. (3)–(7) have been calculated by integrating the relevant collisional cross sections. Table II presents a list of the prevailing electron-neutral reactions. Two vibrational excitation reactions with the thresholds of 0.162 and 0.361 eV[52,53] for the electron collisions with CH_4 molecules were considered in our study. For the inelastic electron C_2H_2 collisions three vibrational excitations with the threshold energies ~ 0.09, 0.255 and 0.407 eV[54,52] have been accounted for. Two vibrational excitations of C_2H_4 with the threshold energies of 0.1 and 0.36 eV[54,52] are also included in the model. Likewise, for electron H_2 collisions we take into account two rotational excitations with the threshold energies of 0.044 and 0.073 eV and three vibrational excitation with the thresholds of 0.516, 1.0, and 1.5 eV.[52] Electronic excitations of Ar, CH_4, C_2H_2, C_2H_4, H_2, and H were accounted for in the power balance Eq. (7). The relevant reaction cross sections can be found elsewhere.[52,55] The number of different vibrational and rotational excitation reactions (noted "vib" and "rot" in Table II) is also shown in Table II.

A list of the neutral–neutral reactions and reaction rate coefficients compiled using the available data[19,20,60,61] are given in Table III (T_g in the Table III is the gas temperature in K). Full data on the rate coefficients for the ion-neutral reactions can be found elsewhere.[18,52,61–63] The corresponding rate constants are shown in Table IV.

The set of Eqs. (2)–(7) has been solved by the time evolution method. To start a numerical cycle we have made an initial guess for the effective electron temperature. It allows one to obtain the average electron energy $\langle \varepsilon \rangle = 3/2 T_{\mathrm{eff}}$ and the rate coefficients entering Eqs. (3)–(7). We note that Eqs. (3)–(7) are the nonlinear and time-dependent equations with respect to the time-varying number densities of different

[This article is copyrighted as indicated in the article. Reuse of AIP content is subject to the terms at: http://scitation.aip.org/termsconditions. Downloaded to] IP: 131.181.251.131 On: Mon, 14 Jul 2014 22:52:45

species $n_i(t)$ and $n_j(t)$. As a result of the linearization of Eqs. (3)–(7), the products $n_i(t)n_j(t)$ are replaced by $n_i(t)n_j(t-\Delta)$, where $n_j(t-\Delta)$ is the neutral/charged particle density at the previous moment of time $(t-\Delta)$. Here, the time step Δ can be chosen empirically to enable the best convergence of the numerical routine. Therefore, the left-hand side of Eqs. (3)–(5) can be presented in the algebraic form $[n_\alpha(t)-n_\alpha(t-\Delta)]/\Delta$. At the initial stage we have used a guessed T_{eff} and plasma-off densities of Ar, CH_4, and H_2. The densities of other nonradical and radical neutrals have been assumed to be zero at this stage.

For the assumed T_{eff}, the number densities of the species have been computed from the linearized Eqs. (3)–(7), the latter set being solved by the conventional Gauss method. At the next temporal step we assume that $n_\alpha(t-\Delta)$ is equal to the as-calculated from the previous step value, and repeat the cycle at fixed T_{eff} until the absolute value of $[n_\alpha(t)-n_\alpha(t-\Delta)]/n_\alpha(t)$ becomes of the order of 10^{-3}. This routine usually requires approximately 250 computation cycles.

Thereafter, solving Eqs. (3)–(7), the corrected densities of H_2 and CH_4, as well as the densities of other species, are calculated. This routine is followed by probing into the plasma quasineutrality condition (2) and proper adjustment of the effective electron temperature and subsequent repetition of any number of cycles until after the above condition has been satisfied.

[1] W. B. Choi, D. S. Chung, J. H. Kang, H. Y. Kim, Y. W. Jin, I. T. Han, Y. H. Lee, J. E. Jung, N. S. Lee, G. S. Park, and J. M. Kim, Appl. Phys. Lett. **75**, 3129 (1999).
[2] S. J. Tans, A. R. M. Verschueren, and C. Dekker, Nature (London) **393**, 49 (1998).
[3] M. B. Nardelli and J. Bernholc, Phys. Rev. B **60**, R16338 (1999).
[4] L. Nilsson, O. Groening, O. Kuettel, P. Groening, and L. Schlapbach, J. Vac. Sci. Technol. B **20**, 326 (2002).
[5] W. Zhu, C. Bower, O. Zhou, G. Kochanski, and S. Jin, Appl. Phys. Lett. **75**, 873 (1999).
[6] M. Su, B. Zheng, and J. Liu, Chem. Phys. Lett. **322**, 321 (2000).
[7] L. Delzeit, B. Chen, A. Cassell, R. Stevens, C. Nguyen, and M. Meyyappan, Chem. Phys. Lett. **348**, 368 (2001).
[8] L. Delzeit, I. McAninch, B. A. Cruden, D. Hash, B. Chen, J. Han, and M. Meyyappan, J. Appl. Phys. **91**, 6027 (2002).
[9] M. Meyyappan, L. Delzeit, A. Cassell, and D. Hash, Plasma Sources Sci. Technol. **12**, 205 (2003), and references therein.
[10] Z. L. Tsakadze, K. Ostrikov, and S. Xu, (in press); Z. Tsakadze, S. Xu, J. Long, and K. Ostrikov, Bull. Am. Phys. Soc. **48**, 13 (2003).
[11] V. I. Merkulov, D. H. Lowndes, Y. Y. Wei, G. Eres, and E. Voelkl, Appl. Phys. Lett. **76**, 3555 (2000).
[12] C. Bower, W. Zhu, S. Jin, and O. Zhou, Appl. Phys. Lett. **77**, 830 (2000).
[13] Y. M. Shyu and F. C. N. Hong, Diamond Relat. Mater. **10**, 1241 (2001).
[14] M. Chen, C. M. Chen, S. C. Shi, and C. F. Chen, Jpn. J. Appl. Phys., Part 1 **42**, 614 (2003).
[15] Z. L. Tsakadze, K. Ostrikov, J. D. Long, and S. Xu (in press).
[16] Y. S. Woo, I. T. Han, Y. J. Park, H. J. Kim, J. E. Jung, N. S. Lee, D. Y. Jeon, and J. M. Kim, Jpn. J. Appl. Phys., Part 1 **42**, 1410 (2003).
[17] T. Hirao, K. Ito, H. Furuta, Y. K. Yap, T. Ikuno, S. Honda, Y. Mori, T. Sasaki, and K. Oura, Jpn. J. Appl. Phys., Part 2 **40**, L631 (2001).
[18] D. Herrebout, A. Bogaerts, M. Yan, R. Gijbels, W. Goedheer, and E. Dekempeneer, J. Appl. Phys. **90**, 570 (2001).
[19] S. F. Yoon, K. H. Tan, Rusli, and J. Ahn, J. Appl. Phys. **91**, 40 (2002).
[20] V. Ivanov, O. Proshina, T. Rakhimova, A. Rakhimov, D. Herrebout, and A. Bogaerts, J. Appl. Phys. **91**, 6296 (2002).
[21] K. Bera, B. Farouk, and Y. H. Lee, Plasma Sources Sci. Technol. **10**, 211 (2001).
[22] K. Bera, B. Farouk, and P. Vitello, J. Phys. D **34**, 1479 (2001).
[23] D. B. Hash and M. Meyyappan, J. Appl. Phys. **93**, 750 (2003).
[24] D. Hash, D. Bose, T. R. Govindan, and M. Meyyappan, J. Appl. Phys. **93**, 6284 (2003).
[25] S. Xu, K. N. Ostrikov, W. Luo, and S. Lee, J. Vac. Sci. Technol. A **18**, 2185 (2000).
[26] S. Xu, K. N. Ostrikov, Y. Li, E. L. Tsakadze, and I. R. Jones, Phys. Plasmas **8**, 2549 (2001).
[27] K. N. Ostrikov, S. Xu, and A. B. M. Shafiul Azam, J. Vac. Sci. Technol. A **20**, 251 (2002).
[28] V. Schulz-von der Gathen, J. Roepcke, T. Gans, M. Kaning, C. Lukas, and H. F. Doebele, Plasma Sources Sci. Technol. **10**, 530 (2001).
[29] C. Riccardi, R. Barni, M. Fontanesi, and P. Tosi, Chem. Phys. Lett. **329**, 66 (2000).
[30] T. Nozaki, K. Okazaki, U. Kortshagen, and J. Heberlein, Bull. Am. Phys. Soc. **48**, 13 (2003).
[31] E. Gogolides, D. Mary, A. Rhallabi, and G. Turban, Jpn. J. Appl. Phys., Part 1 **34**, 261 (1995).
[32] J. Geddes, R. W. McCullough, A. Donnelly, and H. B. Gilbody, Plasma Sources Sci. Technol. **2**, 93 (1993).
[33] K. N. Ostrikov, I. B. Denysenko, E. L. Tsakadze, S. Xu, and R. G. Storer, J. Appl. Phys. **92**, 4935 (2002).
[34] H. Amemiya, J. Phys. Soc. Jpn. **66**, 1335 (1997).
[35] J. T. Gudmundsson, Plasma Sources Sci. Technol. **10**, 76 (2001).
[36] T. Chevolleau and W. Fukarek, Plasma Sources Sci. Technol. **9**, 568 (2000).
[37] N. Sadeghi, M. van de Grift, D. Vender, G. M. W. Kroesen, and F. J. de Hoog, Appl. Phys. Lett. **70**, 835 (1997).
[38] H. Kojima, H. Toyoda, and H. Sugai, Appl. Phys. Lett. **55**, 1292 (1989).
[39] C. Hopf, K. Letourneur, W. Jacob, T. Schwarz-Selinger, and A. Von Keudell, Appl. Phys. Lett. **74**, 3800 (1999).
[40] A. Von Keudell, T. Schwarz-Selinger, M. Meier, and W. Jacob, Appl. Phys. Lett. **76**, 676 (2000).
[41] N. Mutsukura, S. Inoue, and Y. Machi, J. Appl. Phys. **72**, 43 (1992).
[42] C. Hopf, T. Schwarz-Selinger, W. Jacob, and A. Von Keudell, J. Appl. Phys. **87**, 2719 (2000).
[43] C. Lee and M. A. Lieberman, J. Vac. Sci. Technol. A **13**, 368 (1995).
[44] V. A. Godyak, *Soviet Radio Frequency Discharge Research* (Delphic, Falls Church, VA, 1986).
[45] M. Kawase, T. Nakai, A. Yamaguchi, T. Hakozaki, and K. Nashimoto, Jpn. J. Appl. Phys., Part 1 **36**, 3396 (1997).
[46] I. Peres, M. Fortin, and J. Margot, Phys. Plasmas **3**, 1754 (1996).
[47] K. N. Ostrikov, S. Xu, and M. Y. Yu, J. Appl. Phys. **88**, 2268 (2000).
[48] M. Chhowalla, K. B. K. Teo, C. Ducati, N. L. Rupesinghe, G. A. J. Amaratunga, A. C. Ferrari, D. Roy, J. Robertson, and W. I. Milne, J. Appl. Phys. **90**, 5308 (2001).
[49] S. Stoykov, C. Eggs, and U. Kortshagen, J. Phys. D **34**, 2160 (2001).
[50] E. Covacevic, I. Stefanovic, J. Berndt, and J. Winter, J. Appl. Phys. **93**, 2924 (2003).
[51] S. Ashida, C. Lee, and M. A. Lieberman, J. Vac. Sci. Technol. A **13**, 2498 (1995).
[52] http://www.kinema.com/download.htm
[53] D. K. Davies, L. E. Kline, and W. E. Bies, J. Appl. Phys. **65**, 3311 (1989).
[54] M. Hayashi, in *Nonequilibrium Processes in Partially Ionized Gases*, edited by M. Capitelli and J. N. Bardsley (Plenum, New York, 1990).
[55] W. L. Fite and R. T. Brackmann, Phys. Rev. **112**, 1151 (1958).
[56] T. Nakano, H. Toyoda, and H. Sugai, Jpn. J. Appl. Phys., Part 1 **30**, 2912 (1991).
[57] Y.-K. Kim and M. Eugene Rudd, Phys. Rev. A **50**, 3954 (1994).
[58] A. G. Engelhardt and A. V. Phelps, Phys. Rev. **131**, 2115 (1963).
[59] D. A. Alman, D. N. Ruzic, and J. N. Brooks, Phys. Plasmas **7**, 1421 (2000).
[60] M. Heintze, M. Magureanu, and M. Kettlitz, J. Appl. Phys. **92**, 7022 (2002).
[61] K. Tachibana, M. Nishida, H. Harima, and Y. Urano, J. Phys. D **17**, 1727 (1984).
[62] R. L. Mills, P. C. Ray, B. Dhandapani, R. M. Mayo, and J. He, J. Appl. Phys. **92**, 7008 (2002).
[63] H. Chatham, D. Hils, R. Robertson, and A. C. Gallagher, J. Chem. Phys. **79**, 1301 (1983).

[This article is copyrighted as indicated in the article. Reuse of AIP content is subject to the terms at: http://scitation.aip.org/termsconditions. Downloaded to] IP: 131.181.251.131 On: Mon, 14 Jul 2014 22:52:45